Accepted Manuscript

Title: CuInS$_2$ sensitized TiO$_2$ hybrid nanofibers for improved photocatalytic CO$_2$ reduction

Authors: Feiyan Xu, Jianjun Zhang, Bicheng Zhu, Jiaguo Yu, Jingsan Xu

Submit to *Applied Catalysis B: Environmental*

CuInS₂ sensitized TiO₂ hybrid nanofibers for improved photocatalytic CO₂ reduction

Feiyan Xu[a], Jianjun Zhang[a], Bicheng Zhu[a], Jiaguo Yu[a,b,*], Jingsan Xu [c,*]

[a] State Key Laboratory of Advanced Technology for Material Synthesis and Processing, Wuhan University of Technology, Luoshi Road 122, Wuhan 430070, P. R. China,

E-mail: **jiaguoyu@yahoo.com**

[b] Department of Physics, Faculty of Science, King Abdulaziz University, Jeddah 21589, Saudi Arabia

[c] School of Chemistry, Physics and Mechanical Engineering, Queensland University of Technology, Brisbane, Queensland 4000, Australia.

E-mail: **jingsan.xu@qut.edu.au**

Graphical abstract
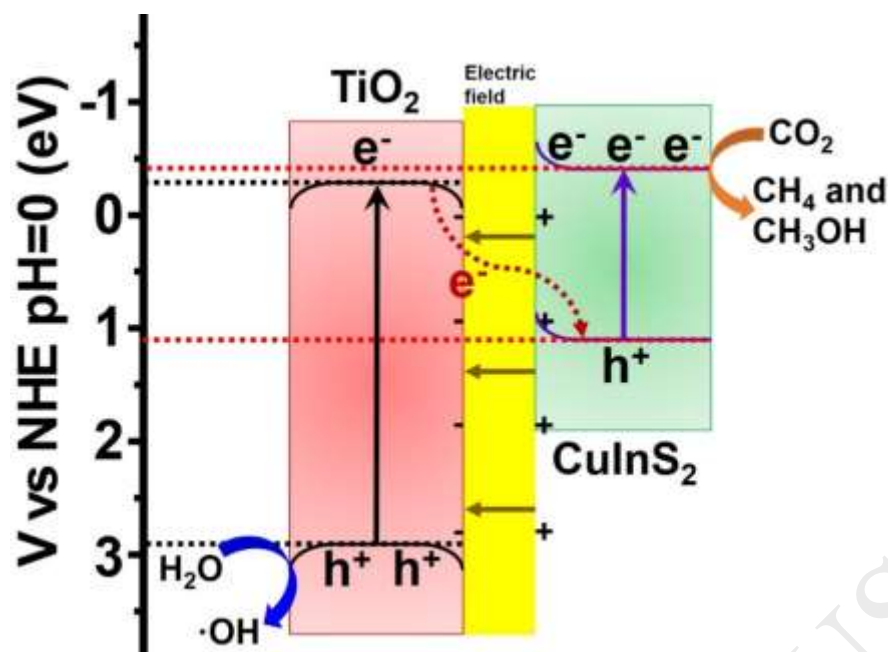
A novel TiO_2/$CuInS_2$ hybrid is synthesized by an *in-situ* hydrothermal approach, with the

TiO_2 naonfibers coated by few-layer $CuInS_2$ nanoplates. A direct Z-scheme heterojunction is

generated between TiO_2 and $CuInS_2$ which results in superior photocatalytic activity for CO_2

reduction under irradiation.

Highlights

1. In-situ deposition of $CuInS_2$ nanoplates onto TiO_2 nanofibers.

2. Direct Z-scheme TiO_2/$CuInS_2$ heterostructure was generated.

3. The prepared photocatalyst with enhanced photocatalytic CO_2 reduction activity.

4. The photocatalytic mechanism investigated by XPS and DFT calculation.

Abstract

Photocatalytic CO_2 reduction into solar fuels over photocatalysts has theoretically and

practically become a hot research topic. Herein, we fabricated a novel hybrid TiO_2 nanofiber

coated by $CuInS_2$ nanoplates through a hydrothermal method. The materials were

characterized by X-ray diffraction, electron microscopes, UV-vis absorption spectra, nitrogen

sorption, X-ray photoelectron spectroscopy and electrochemical impudence spectroscopy.

The resulting $TiO_2/CuInS_2$ hybrid nanofibers exhibit superior photocatalytic activity for CO_2

reduction under irradiation, due to the generation of direct Z-scheme heterojunction between

TiO_2 and $CuInS_2$. This work may provide an alternate methodology to design and fabricate

multicomponent TiO_2-based photocatalyst for high-efficiency CO_2 photoreduction.

1. Introduction

Photocatalytic CO_2 reduction over well-designed catalysts has been considered an emerging

way for recycling CO_2 back to renewable fuels, e.g., CH_4 and CH_3OH with the aid of solar

energy, which is regarded as one of the most promising strategies to overcome the energy and

environmental crises [1-7]. For example, metal-organic frameworks (MOF), a type of

micro-mesoporous hybrid materials, are recently emerging as a new category of materials for

CO_2 photo-reduction due to their special structural characteristics and remarkable adsorption

capability for CO_2 [8-10]. Besides, TiO_2 as a typical semiconductor photocatalyst, has been

frequently studied for CO_2 reduction due to its high stability, nontoxicity and abundant

availability [11-14]. However, TiO_2 can only absorb UV-light because of its large band gap

[15, 16]. Moreover, it shows a fast recombination of the photogenerated electron-hole pairs,

which leads to low photocatalytic performance [17-19]. Several approaches have been

explored to improve the photocatalytic activities of TiO_2, including noble metal deposition

(*e.g.* Pt, Au, Pd, Ag) [20-24], nonmetal doping (*e.g.* N, C) [25-28], surface sensitization [29,

30], coupling with narrow-bandgap semiconductors (*e.g.* CdS, g-C_3N_4, Cu_2O) [31-36] and so

on. Among these, hybridizing TiO_2 with other semiconductors is believed to be an effective

method to broaden the light absorption and meanwhile improve the separation and extraction

of the photogenerated carriers.

Differing from TiO_2, $CuInS_2$ has a narrow direct band gap of 1.50 eV, close to the optimal

band gap (1.45 eV) for solar light harvesting [37-39], and meanwhile shows an ultrahigh

absorption coefficient (1×10^5 cm^{-1}). Besides, $CuInS_2$ shows a pronounced defect tolerance

and exceptional radiation hardness as compared to other semiconductors [40-42]. $CuInS_2$

does not contain any toxic heavy metals and has been investigated for photovoltaics [43],

bioimaging [44], and photocatalytic water splitting [45]. For instance, Kudo and coworkers

have prepared a ZnS-$CuInS_2$-$AgInS_2$ ternary solid solution which exhibited 7.4% quantum

yield of hydrogen production under 520 nm irradiation [45]. In addition, $CuInS_2$ has been

combined with other semiconductors to make composite photocatalysts, such as

MoS_2/$CuInS_2$ [46], g-C_3N_4/$CuInS_2$ [47], Bi_2WO_6/$CuInS_2$ [48] and ZnO/$CuInS_2$ [49, 50], for

enhanced H_2 generation from water splitting or organic pollutants degradation. In these cases,

$CuInS_2$ was presented as nanosheets or quantum dots. It is also reported that $CuInS_2$ thin

films can function as cathodes for photoelectrochemical reduction of CO_2 [51]. However,

4

$CuInS_2$ involved photocatalysts for direct CO_2 reduction have been rarely demonstrated and more efforts are required to improve the solar driven CO_2-to-fuel conversion efficiency.

Herein, we report the facile synthesis of TiO_2 nanofibers sensitized with $CuInS_2$ nanoplates through an *in-situ* hydrothermal process. The obtained $TiO_2/CuInS_2$ hybrid nanofibers show increased optical absorption and enhanced charge separation, and thus improved photocatalytic CO_2 reduction was achieved. Based on the experimental data and DFT calculation, we propose a direct Z-scheme heterojunction formed between the TiO_2 nanofiber and the $CuInS_2$ nanoplates.

2. Experimental details

2.1. Materials and synthesis of electrospun TiO$_2$ nanofibers

Poly(vinyl pyrrolidone) with an average molecular weight of 1300000 was purchased from Tianjin Bodi Chemical Co., Ltd. The other chemicals were of analytical grade and purchased from Shanghai Chemical Company. Electrospun TiO_2 nanofibers were prepared according to our previous work [11]. Typically, 2.0 g of Tetrabutyl titanate (TBT) and 0.75 g of PVP were dissolved in the solvent containing 10.0 g of ethanol and 2.0 g of acetic acid. The mixture became a transparent light yellow solution after magnetically stirring for 5 h at room temperature. The solution was then poured into a 10 mL syringe in the electrospinning setup. The steel needle had a distance of 10 cm and a voltage of 15 kV with respect to the static collector. And the solution feeding rate is maintained at 2.5 mL·h^{-1}. The collected electrospun samples (TiO_2 precursors) were calcinated at 550 °C in air for 2 h with a ramping rate of 2 °C·min^{-1}.

2.2. Preparation of TiO$_2$/CuInS$_2$ heterostructures

TiO_2 nanofibers were first chemically etched to increase surface roughness. Briefly, TiO_2 nanofiber was immersed in a concentrated NaOH solution (10 M) at 160 °C for 15 min, and washed with dilute HCl solution and water for several times. As-etched TiO_2 fibers were then annealed at 450 °C in air for 1 h with a ramping rate of 2 °C min^{-1}. The rough TiO_2 nanofibers are labeled as T.

$TiO_2/CuInS_2$ heterostructures were synthesized through a hydrothermal method. Typically, a transparent solution was formed by mixing 0.0125 mmol $Cu(NO_3)_2$ (the mass ratio of $CuInS_2$ was 1 wt. %), 0.0125 mmol $In(NO_3)_2$ and 0.025 mmol L-cysteine hydrochloride with 80 mL deionized water. Then 0.1 g TiO_2 nanofibers were added to the above solution under vigorous stirring. The obtained suspension was transferred to a Teflon cup of 100 mL inner volume in a stainless steel-lined autoclave. The autoclave was maintained at 160 °C for 12 h and then was allowed to cool to room temperature. The solid product was washed with deionized water and ethanol several times and dried at 80 °C for 4 h to obtain $TiO_2/CuInS_2$ heterostructures. For comparison, $TiO_2/CuInS_2$ samples with various mass ratios of $CuInS_2$ were synthesized by varying the amount of $Cu(NO_3)_2$ from 0.03, 0.06 to 0.12 mmol while fixing the molar ratio of $Cu(NO_3)_2$: $In(NO_3)_2$: L-cysteine hydrochloride at 1:1:2. The nominal mass ratios of $CuInS_2$ were 2.5 wt.%, 5 wt.% and 10 wt.%, respectively. These $TiO_2/CuInS_2$ samples were labeled as TC_x (x = 1, 2.5, 5, 10). The actual compositions of the samples were determined by inductively coupled plasma atomic emission spectrometry (ICP-AES) by using a Prodigy 7 spectrometer (see Table 1)

2.3. Characterization

The X-ray diffraction (XRD) patterns were recorded on a D/Max-RB X-ray diffractometer

6

(Rigaku, Japan) with Cu $K\alpha$ radiation ($\lambda = 0.15418$ nm) with a scan rate (2θ) of 0.05 $°\cdot s^{-1}$.

The morphology was observed on a JSM 7500F field emission scanning electron microscope

(FESEM). Transmission electron microscopy (TEM) images and energy dispersive X-ray

(EDX) spectrometer were recorded on a Titan G2 60-300 electron microscope. Nitrogen

adsorption-desorption data were recorded on a Micromeritics ASAP 3020 nitrogen adsorption

apparatus (USA) at 77 K. Prior to measurements, the samples were degassed at 150 °C for 12

h. The specific surface areas (S_{BET}) calculated by the Brunauer-Emmett-Teller (BET) method

using adsorption data in a relative pressure range from 0.05 to 0.3. The total pore volumes

were estimated from nitrogen adsorption volume adsorbed at the relative pressure of 0.97.

The pore size distributions were calculated from desorption data of isotherms using the

Barret-Joyner-Halender (BJH) method. UV-visible diffuse reflectance spectra of samples

were recorded on a Shimadzu UV-2600 UV-visible spectrophotometer (Japan) using $BaSO_4$

as a reference. X-ray photoelectron spectroscopy (XPS) measurements were conducted on a

Thermo ESCALAB 250Xi instrument with Al $K\alpha$ X-ray radiation. The binding energy was

calibrated with reference to C 1s signal (284.8 eV).

2.4. Photoelectrochemical measurements

The photoelectrochemical measurements were conducted in 0.5 M Na_2SO_4 aqueous solution

on a CHI660C electrochemical workstation (Shanghai CH Instruments), with a 3W LED

lamp (365 nm) as the light source. A Pt wire and saturated Ag/AgCl electrode were used as

counter and reference electrodes, respectively. For preparing the working electrode, 80 mg of

the photocatalysts (T, TC1, TC2.5, TC5 and TC10) were ground with 1.0 mL ethanol to form

a slurry. The slurry was blade-coated onto a 2 cm × 1.5 cm F-doped SnO_2-coated (FTO) glass

with an active area of 1 cm^2, followed by drying at 100 °C for 1 h. All the electrodes used had

a similar thickness. The EIS measurements was carried out by applying the bias of the open

circuit potential and recorded over a frequency range of 0.01-10^5 Hz with an ac amplitude of

10 mV.

2.5. Analysis of hydroxyl radicals (·OH)

A terephthalic acid (TA) fluorescence probe method was used to quantitatively analyze the

production of ·OH. Typically, 0.1 g of photocatalyst was dispersed in a 20 mL solution

containing 0.5 mM TA and 5 mM NaOH. The suspension was placed in a

dish with a diameter of 9 cm. A 350 W Xe arc lamp (Zhenjian Silver Jewelry Chemical,

China) was positioned 25 cm above the dish. The light intensity on the solution was measured

to be 2.0 mW cm^{-2} with a UV radiometer with the peak intensity of 365 nm (model: UV-A,

Photoelectric Instrument Factory of Beijing Normal University). TA easily reacts with ·OH

and produces a highly fluorescent 2-hydroxyterephthalic acid (TAOH). The amount of ·OH

was determined by measured the concentration of TAOH (fluorescence peak at 425 nm with

an excitation wavelength of 315 nm) using a Hitachi F-7000 fluorescence spectrophotometer

after centrifugation.

2.6. Photocatalytic reduction of CO$_2$

The photocatalytic reduction of CO$_2$ was carried out in a 200 mL home-made Pyrex reactor

with two openings. A 350 W simulated solar Xe arc lamp was used as the light source and

positioned 10 cm above the reactor. A suspension was firstly placed in the reactor by

ultrasonically mixing 50 mg of the catalyst and 10 mL of deionized water. After drying at

80 °C for 2 h, the catalyst formed a uniform film coating on the bottom of the reactor. Prior to

8

irradiation, the reactor was purged with nitrogen for 30 min to ensure an anaerobic

circumstance. CO_2 together with H_2O vapor was in-situ produced through the reaction of

$NaHCO_3$ (0.12 g, introduced into the reactor before seal) and the injected H_2SO_4 solution

(0.25 mL, 2 M). The product (1 mL) was automatically collected at given intervals (1 h) and

analyzed using a Shimadzu GC-2014C gas chromatograph (Japan) equipped with an FID

detector and a methanizer. Blank experiments in the absence of CO_2 or light irradiation

confirmed the CO_2 and light were the key factors for the CO_2 reduction. Control experiment

was also performed to determine whether the carbon resource came from CO_2.

$^{13}CO_2$ isotope tracer experiment was conducted to verify the carbon source of the products

by using ^{13}C isotope-labelled sodium bicarbonate ($NaH^{13}CO_3$, Cambridge Isotope

Laboratories Inc., USA) and H_2SO_4 aqueous solution for the photocatalytic examinations.

After 1 h of photocatalytic reaction, 500 μL of mixed gas was taken out from the reactor and

examined by a gas chromatography-mass spectrometer (GC-MS) (6980N network GC

system-5975 inert mass selective detector, Agilent technologies, USA) to analyze the

products.

2.7. Computational details

The density functional theory (DFT) calculations were performed by using the Cambridge

Serial Total Energy Package (CASTEP). Generalized gradient approximation (GGA) with the

Perdew-Burke-Ernzerhof (PBE) functional was utilized to describe the exchange-correlation

interaction. The energy cutoff and Monkhorst-Pack k-point mesh were set to as 440 eV and 7

$\times$ 7 $\times$ 1, respectively. During the geometry optimization, the convergence tolerance was set as

1.0×10^{-5} eV/atom for energy and 0.03 eV/Å for maximum force. For the construction of

surface models, a vacuum of 20 Å was used to eliminate interactions between periodic

images. The geometric structures of TiO_2 (101) surface and $CuInS_2$ (004) surface are

illustrated in Figure 1. The work function is defined as $\Phi = E_V - E_F$, where E_V and E_F are the

electrostatic potentials of the vacuum and Fermi levels, respectively.
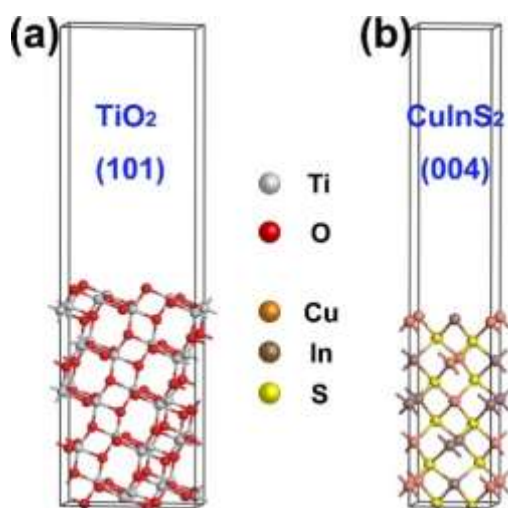
Figure 1. Geometric structure of (a) TiO_2 (101) surface and (b) $CuInS_2$ (004) surface. The

grey, red, orange, brown and yellow spheres stand for Ti, O, Cu, In and S atoms, respectively.

3. Results and discussion

3.1 Crystalline phase and morphology of materials

Figure 2 shows the XRD patterns of the resultant samples with various loadings of $CuInS_2$.

For the original TiO_2 nanofibers, the diffraction peaks can be assigned to anatase TiO_2

(JCPDS file No. 21-1272) or rutile TiO_2 (JCPDS file No. 21-1276). No other diffraction

peaks were observed for TC1 and TC2.5 because of the quite low loading of $CuInS_2$. In

contrast, TC5 and TC10 which had higher loadings of $CuInS_2$ show a new diffraction peak at

around 32.1°, which correspond to the (004) plane of tetragonal $CuInS_2$ (JCPDS file

No.85-1575). The results confirm the formation of $CuInS_2$ by hydrothermal deposition, which

can be further verified by TEM observation below.
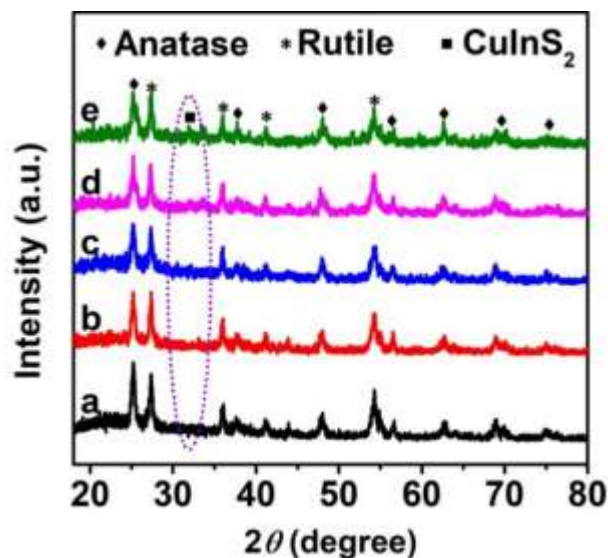
Figure 2. XRD patterns of the samples: (a) T, (b) TC1, (c) TC2.5, (d) TC5 and (e) TC10.

The morphologies of the resultant samples were investigated by SEM and TEM. The SEM image of the pristine TiO_2 before and after NaOH etching was shown in Figure 3a and b, illustrating nanofibers with diameters around 150 nm and lengths of tens of micrometers. After the hydrothermal growth, $CuInS_2$ nanoplates were deposited onto the TiO_2 nanofibers, as shown in Figure 3c and d. The very thin $CuInS_2$ nanoplates had high surface area and more active sites can be exposed, which will be highly favourable for the photocatalytic reactions. The microstructure of the $TiO_2/CuInS_2$ hybrid can be further revealed by TEM image (Figure 3e), showing a TiO_2 nanofiber coated by $CuInS_2$ nanoplates with thickness of ca. 10 nm.
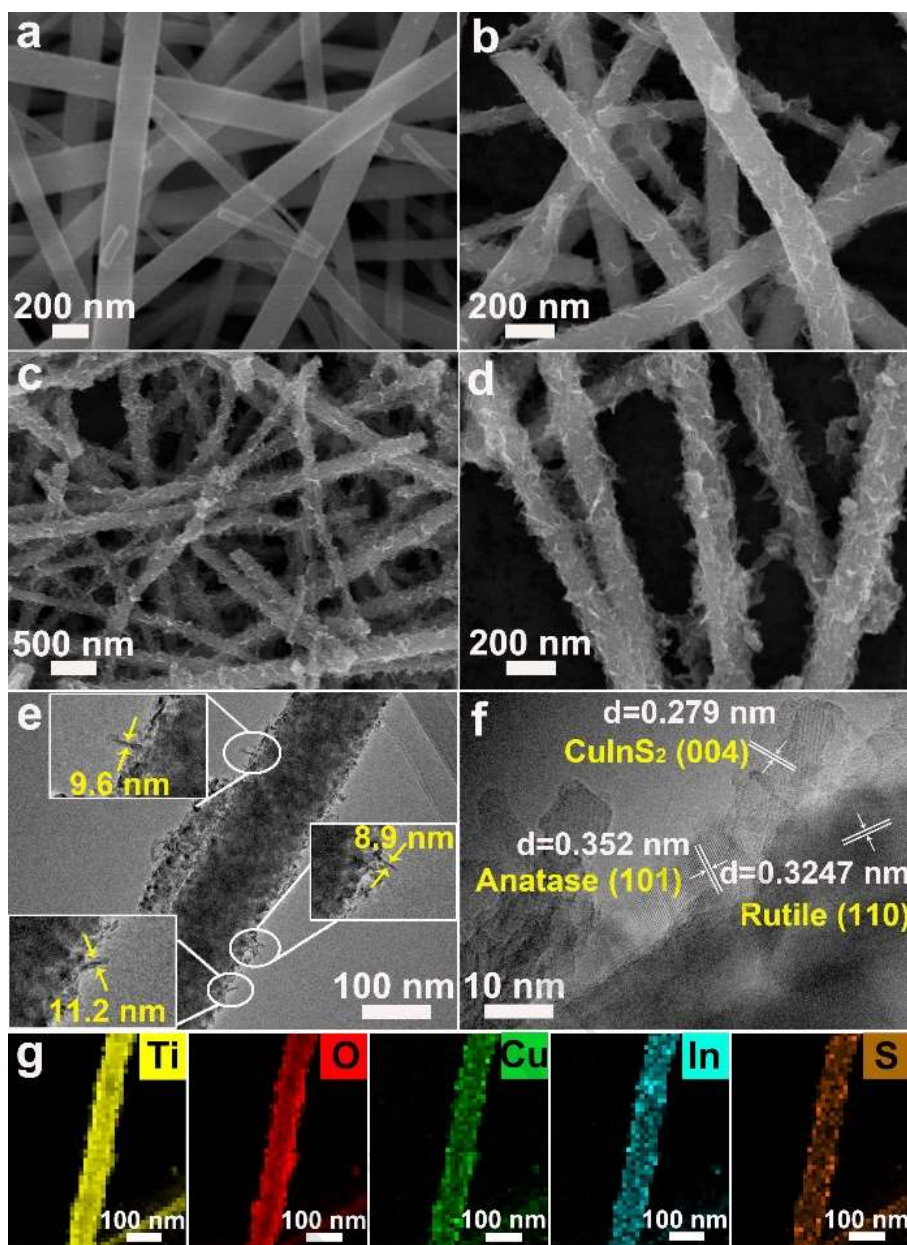
Figure 3. SEM images of (a-b) T and (c-d) TC2.5. TEM image (e) and HRTEM image (f) of

TC2.5. EDX element mappings of (g) Ti, O, Cu, In and S elements for TC2.5.

The crystalline phase of the hybrid material was also examined by high-resolution TEM

(HRTEM). As shown in Figure 3f, the lattice fringes with a spacing of 0.352 and 0.324 nm

corresponded to the (101) plane of anatase TiO_2 and (110) plane of rutile TiO_2, respectively.

In addition, lattice fringes with a spacing of 0.279 nm were also observed, which was

attributed to the (004) plane of $CuInS_2$. The HRTEM analysis further confirmed the

generation of CuInS$_2$ over the TiO$_2$ nanofibers, agreeing with the XRD results as above. The

EDX mapping (Figure 3g) of the nanofiber indicates the co-existence of Ti, O, Cu, In and S

elements, resulting from the heterostructured TiO$_2$/CuInS$_2$ composite.

3.2 UV-vis absorption and nitrogen sorption

UV-vis diffuse reflectance spectra were measured to study the optical absorption properties of

the samples, as shown in Figure 4. As expected, the pristine TiO$_2$ sample can only absorb UV

light (wavelength below 400 nm). After deposition of CuInS$_2$, the hybrid nanofibers show

enhanced visible-light absorption with the increased loading of CuInS$_2$, resulting from the

low bandgap and strong absorption capability of the CuInS$_2$ nanoplates. The significantly

improved optical absorption of the hybrid can potentially result in higher photocatalytic

activity for CO$_2$ reduction, as described below.

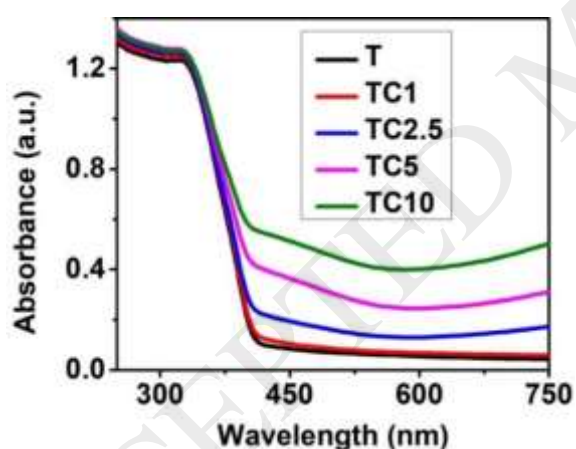**Figure 4.** Diffuse reflectance spectra of the samples.

Figure 5 shows the nitrogen adsorption-desorption isotherms and the corresponding pore

size distribution curves (inset) for T, TC1, TC2.5, TC5 and TC10. All the isotherms can be

identified as type IV according to the BDDT (Brunauer, Deming, Deming and Teller)

classification and having H3-type hysteresis loops at P/P_0 between 0.45 and 0.9, indicating

13

the presence of narrow slit-shaped mesopores that may originate from the random distribution

of $CuInS_2$ nanoplates on the TiO_2 nanofibers [52]. The inset of Figure 5 shows the

corresponding pore size distributions of the samples calculated according to the desorption

isotherms. All the samples show mesoporous structures with the pore size increasing from

~10 nm to ~20 nm after the coating of to the $CuInS_2$ nanoplates. Table 1 summarizes the

specific surface areas (S_{BET}), pore volumes and pore sizes of the samples. The S_{BET} of the

samples shows a volcano shape and reaches the maximum value of 102 $m^2 \cdot g^{-1}$ for TC2.5, as

the loading of $CuInS_2$ was increased.

Table 1. Physical properties of the samples

Samples	$CuInS_2$ mol%	S_{BET} (m^2/g)	PV (m^3/g)	APS (nm)
T	-	43	0.14	10
TC1	1.4	68	0.18	10.4
TC2.5	3.1	102	0.45	17.6
TC5	5.2	83	0.45	21.5
TC10	9.4	51	0.25	20.1

PV: Pore volume, APS: average pore size

Figure 5. Left: nitrogen adsorption-desorption isotherms (inset: pore size distributions) of the

samples. Right (Table 1): specific surface area (S_{BET}), pore volume (PV) and average pore

size (APS) derived from the isotherms.

3.3 XPS analysis
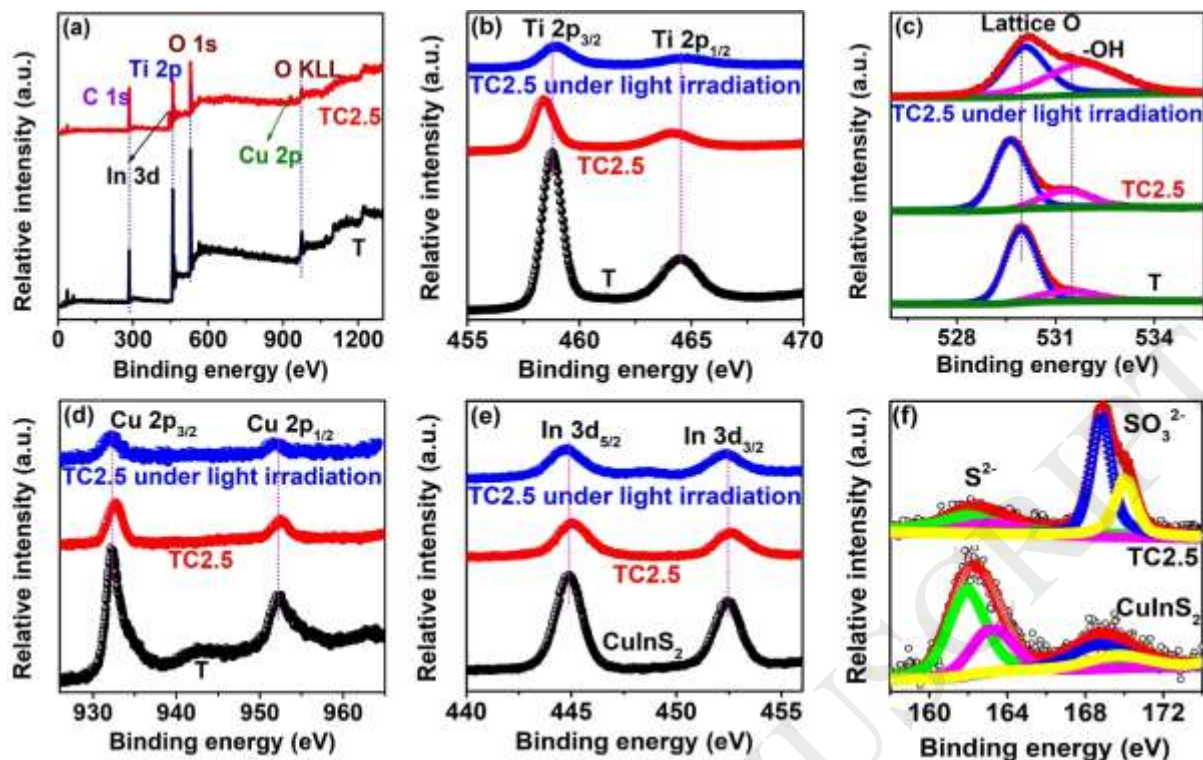
Figure 6. (a) XPS survey spectra of T and TC2.5. XPS spectra of (b) Ti 2p and (c) O 1s of T and TC2.5. XPS spectra of (d) Cu 2p, (e) In 3d and (f) S 2p of $CuInS_2$ and TC2.5.

The surface composition and chemical states of the resultant samples were investigated by XPS. The survey XPS spectrum (Figure 6a) shows the presence of Cu and In elements for TC2.5, in addition to Ti and O, confirming the generation of $CuInS_2$. Figure 6b shows the high-resolution Ti 2p spectrum with two symmetrical peaks corresponding to Ti $2p_{3/2}$ at 458.8 eV and Ti $2p_{1/2}$ at 464.5 eV, respectively. The O 1s XPS spectra of both samples (Figure 6c) can be deconvoluted to lattice oxygen (529.8 eV) in TiO_2 and –OH species (531.6 eV). Note that the binding energies of both Ti 2p and O 1s for TC2.5 shifted by 0.5 eV to lower values as compared to T, suggesting the presence of electron transfer from $CuInS_2$ to TiO_2 after hybridization, which will build an internal electric field at the interface of the hybrid. The directed electron transfer between the two components of the hybrid can be further verified

15

by the DFT calculation shown below. The electron transfer and the associated electric field would play a role in the heterojunction formation and hence affect the photocatalytic activities for CO_2 reduction.

The Cu 2p XPS spectrum of TC2.5 shown in Figure 6d contained two signals at 932.0 and 951.5 eV, corresponding to Cu $2p_{3/2}$ and Cu $2p_{1/2}$, respectively. The two strong photoelectron signals at 444.8 and 452.3 eV in the In 3d XPS spectrum (Figure 6e) of TC2.5 were assigned to In $3d_{5/2}$ and In $3d_{3/2}$, respectively. For comparison, the XPS of pure $CuInS_2$ were also measured and shown in Figure 6d-f. The binding energies of Cu and In for TC2.5 showed clear shift to higher values compared to those of $CuInS_2$, implying the electron transfer from $CuInS_2$ to TiO_2, which agree with the above analysis and suggest the formation of bulid-in electric field and direct Z-scheme heterojunction between them, as detailed below. Figure 6f shows the XPS signal of sulfur, which can be assigned to the presence of S^{2-} and SO_3^{2-} species. Apparently, S^{2-} derived from the formation of $CuInS_2$, and SO_3^{2-} may be generated during the disproportionation of L-cysteine hydrochloride. The results further prove the existence of $CuInS_2$ in TC2.5, which are in good agreement with the XRD and HRTEM analyses.

3.4 Photocatalytic CO_2 reduction and in-situ DRIFTS measurement

For the photocatalytic CO_2 reduction tests, control experiments were first conducted in the absence of photocatalysts, carbon source, irradiation or H_2O (N_2 was used as the reference gas). We found that hydrocarbons were produced only in the presence of the photocatalysts, irradiation, H_2O and CO_2, which verified that the hydrocarbons resulted exclusively from the photoreduction of CO_2. Here, CO_2 can be reduced to CH_4 and CH_3OH upon the as-prepared

16

materials under Xe lamp irradiation. Figure 7a shows the yields of CH_4 and CH_3OH after 1 h of irradiation over the samples. It can be seen that the hydrocarbon yield increased with the loading of $CuInS_2$ and reached a maximum value over TC2.5, with the production rate of 2.5 $\mu mol\, h^{-1}\, g^{-1}$ for CH_4 and 0.86 $\mu mol\, h^{-1}\, g^{-1}$ for CH_3OH. We consider the improvements resulted from the enhanced light absorption, increased surface area and possible improved charge separation and extraction after the growth of $CuInS_2$. We note that the generation rate of CH_4 by TC2.5 almost doubled the generation rate by T, while the yield of CH_3OH only showed a minor increase. Further rising of the $CuInS_2$ amount would result in a decrease of photocatalytic efficiency (sample TC5 and TC10).

We note that the product (CH_4 and CH_3OH) distribution of CO_2 reduction over $TiO_2/CuInS_2$ varied with the loading amount of $CuInS_2$. From the thermodynamic point of view, the reduction potential of $CO_2 \rightarrow CH_4$ (-0.24 V vs. NHE, pH7) is more positive than that of $CO_2 \rightarrow CH_3OH_4$ (-0.38 V vs. NHE, pH7). We speculate that with increasing amount of $CuInS_2$, more electrons can be generated and/or transferred to react with CO_2 molecules. Meanwhile, since the $CO_2 \rightarrow CH_4$ is energetically more favourable than $CO_2 \rightarrow CH_3OH_4$ as mentioned above, the CH_4 generation rate was improved with the loading of $CuInS_2$, and meanwhile the generation rate of CH_3OH remained unchanged.
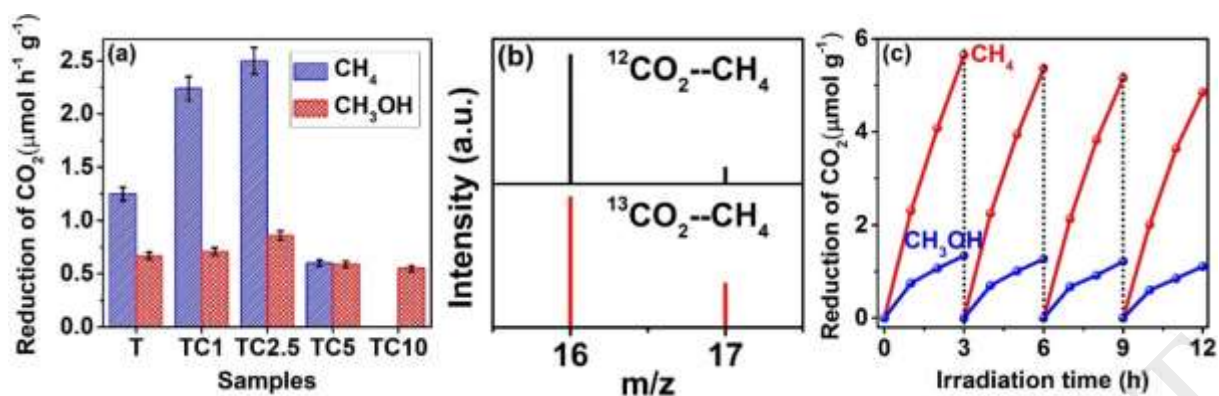
17

Figure 7. (a) Photocatalytic activities of the CO_2 reduction over different photocatalysts. (b) The GC-MS patterns of the produced CH_4 over TC2.5 using $^{12}CO_2$ and $^{13}CO_2$ as the carbon source, respectively. (c) The long-term photocatalytic activities of TC2.5 for CO_2 reduction.

Further, to verify the real carbon source of the photocatalytic products, isotope tracer experiment involving photo-reduction of $^{13}CO_2$ ($^{12}CO_2$ was also tested as a reference) was conducted and examined by GC-MS. As shown in Figure 7b, a strong peak assigned to $^{13}CH_4$ (m/z = 17) was clearly observed when using $^{13}CO_2$ as the carbon source, while the corresponding peak using $^{12}CO_2$ as the carbon source was much weaker. These results confirmed that the detected products over the as-prepared photocatalyst originated from the CO_2 source gas rather than any residual/contaminant carbon species.

Table 2. Photocatalytic CO_2 reduction performances of various TiO_2-based photocatalysts.

Photocatalyst	Reductant	Light	Product	Yield ($\mu mol\ g^{-1}\ h^{-1}$)	Ref.
2.5 % $CuInS_2/TiO_2$	H_2O vapor	350 W Xe lamp	CH_4	2.5	This work
			CH_3OH	0.86	
$CuIn_2S_4$-0.33/TiO_2	H_2O vapor	300 W Xe lamp	CH_4	1.135	[53]
Pt/TiO_2	H_2O vapor	300 W Xe lamp	CH_4	4.8	[54]
			CO	0.1	
1.5 % Ag/TiO_2	H_2O vapor	300 W Xe lamp	CH_4	1.4	[55]
$Pt-Cu_2O/TiO_2$	H_2O vapor	300 W Xe lamp	CH_4	1.42	[56]
			CO	0.05	

18

Ag-Mn-N/TiO$_2$	H$_2$O vapor	300 W Xe arc lamp	CH$_3$OH	0.53	[26]
5 wt.% GO/TiO$_2$	H$_2$O vapor	500 W Xe arc lamp	CH$_4$	0.5	[17]
			CO	1.86	
			C$_2$H$_6$	0.05	
			C$_2$H$_4$	0.51	
A/R-TiO$_2$	H$_2$O vapor	100 W Xe lamp	CH$_4$	1.13	[57]
TiO$_2$ flakes	H$_2$O liquid	300 W Hg lamp	Formate	1.9	[58]

Table 2 shows the photocatalytic CO$_2$ reduction performance of various TiO$_2$-based

photocatalysts. It can be found that the TiO$_2$/CuInS$_2$ hybrid exhibits higher or comparable

photocatalytic CO$_2$ conversion activities compared with most of the recently reported

TiO$_2$-based photocatalysts. There are few materials showing higher CO$_2$ reduction efficiency,

nevertheless, these photocatalysts were modified with noble metals such as Pt and Ag, which

increased the cost and limited the large-scale usage. Further, the long-term stability of the

TiO$_2$/CuInS$_2$ hybrid was checked and we found that the photocatalytic CO$_2$ reduction rate

was largely remained after 12 hours illumination (Figure 7c). Therefore, the easily-prepared,

noble-metal-free cocatalyst of CuInS$_2$ can still be of great interest for achieving

high-efficiency CO$_2$ reduction.

Further, we conducted in-situ DRIFTS measurement to explore the CO$_2$ photoreduction

mechanism over TC2.5. As shown in Figure 8, no absorption bands can be found in the

absence of CO$_2$ and H$_2$O (Figure 8a) in the dark. When CO$_2$ and water vapor were

introduced into the reactor for 20 minutes in the dark, the molecules can be adsorbed onto

TC2.5, evidenced by the presence of the monodentate bicarbonate species at 1650 cm^{-1}

(v_{as}(CO$_3$)) and 1420 cm^{-1} (v_s(CO$_3$)) as well as bidentate bicarbonate species at 1515 cm^{-1}

(v_{as}(CO$_3$)) and 1395 cm^{-1} (v_s(CO$_3$)) [59-61] (Figure 8b). The absorption spectra showed no

changes when the exposure time was further increased to 40 and 60 minutes (Figure 8c-d)

without illumination. Under the photoirradiation, the intensities of monodentate and

bidentate bicarbonate species increase with irradiation time (Figure 8e-g) due to the large

thermodynamic tendency for the conversion of CO_2 to CO_3^{2-}. Meanwhile, some new

absorption bands appear at 1540 and 1340 cm^{-1}, which are attributed to $\nu_{as}(CO_2)$ and

$\nu_s(CO_2)$ of bidentate formic acid species [59]. The absorption bands located at 1456 and

1365 cm^{-1} are assigned to $\nu_{as}(COO)$ and $\nu_s(COO)$ of absorbed formic acid species [60]. The

bands at 1699 and 1740 cm^{-1} can be ascribed to $\nu_{as}(CO)$ of absorbed formate and formic

acid species, respectively [61]. It can be concluded that formate and formic acid were

generated as the intermediates on the surface of $TiO_2/CuInS_2$ nanohybrids during the CO_2

reduction.
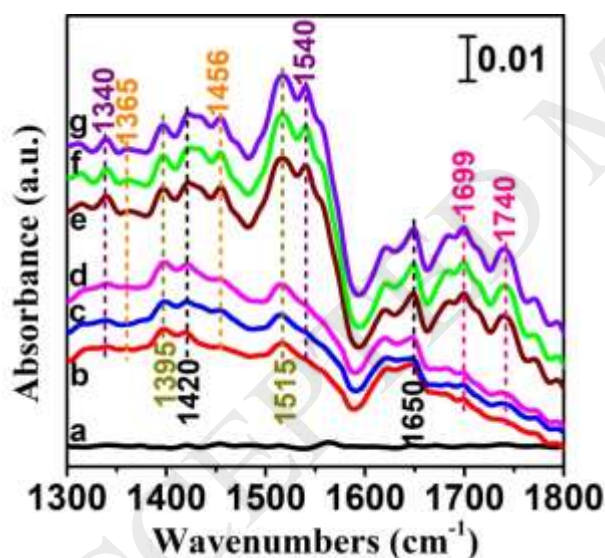
Figure 8. In-situ DRIFTS spectra of TC2.5 under the flow CO_2/H_2O: (a) in the absence of

CO_2/H_2O in the dark, (b-d) after the introduction of CO_2/H_2O for 20, 40 and 60 minutes in

the dark, and (e-g) after the photo-irradiation for 20, 40 and 60 minutes.

3.5 EIS measurement, EPR analysis and DFT calculation

Electrochemical impedance spectra (EIS) were measured to investigate the photogenerated

charge transfer dynamics. Figure 9 shows the EIS spectra of the samples and the semicircles

observed in the Nyquist plots correspond to the charge transfer resistance in the

sample/electrode interface. In general, a smaller semicircle implies a better charge transfer

across this interface. As can be seen, the semicircle became smaller as the content of $CuInS_2$

was increased, indicating that the hybridization with $CuInS_2$ was able to improve the electron

transfer which thus led to a significant photocatalytic enhancement for the CO_2 reduction.
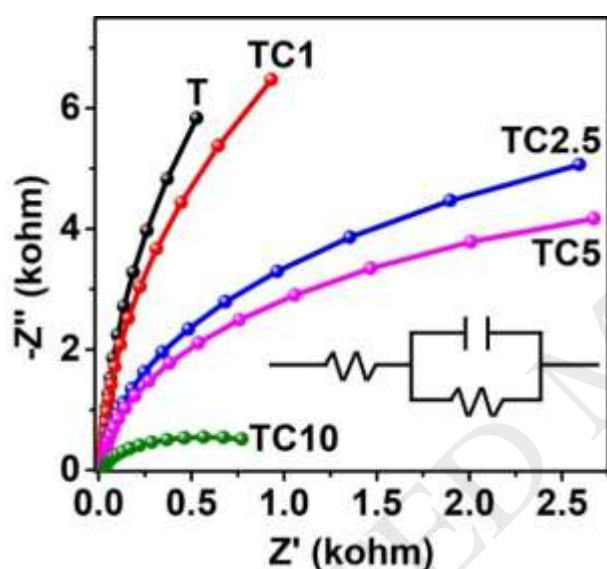
Figure 9. Nyquist plots of the samples measured in 0.5 M Na_2SO_4 aqueous solution under Xe

lamp irradiation.

Moreover, terephthalic acid (TA) was used as a probe molecule to examine the ·OH free

radicals produced over the samples under illumination. The ·OH radicals can easily react with

TA to produce a luminescent TAOH adduct, with fluorescence emission centered at 425 nm.

Hence, the corresponding photoluminescence (PL) spectra recorded after UV illumination for

different time (0~60 min) over TC2.5 were recorded and shown in Figure 10a. The PL

intensity boosted with increasing irradiation time, implying the continuous generation of

hydroxyl radicals upon TC2.5 under illumination. Figure 10b shows the time courses of the

PL intensity from TAOH for different samples. Clearly, TC2.5 generated the highest amount

of ·OH as compared to other samples and in contrast, while T showed minor PL increase

even after 60 min illumination. Based on these results, we proposed a direct Z-scheme

heterojunction formed between TiO_2 and $CuInS_2$, i.e. the photo-generated electrons in the

conduction band of TiO_2 can transfer to the valence band of $CuInS_2$, reducing the

recombination rate of electron/hole pairs and facilitating the production of ·OH in aqueous

solution. In the process of CO_2 reduction, we suppose that the ·OH radicals were captured

and quenched by the hydroxyl groups from TiO_2 [62, 63].
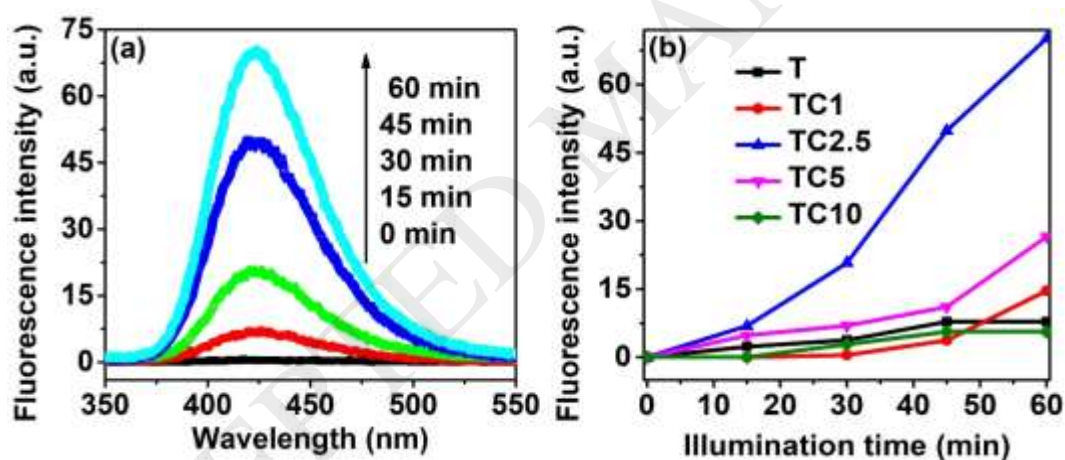
Figure 10. (a) PL spectra of TA aqueous solution (5×10^{-4} M) in the presence of TC2.5 upon

illumination for 0, 15, 30, 45 and 60 min. (b) PL intensity variation (425 nm) of the TA

aqueous solution against time in the presence of different samples.

The Z-scheme charge transfer pathway can be more directly evidenced by in-situ XPS

measurement under light irradiation. As shown in Figure 6b and c, the binding energies of Ti

2p and O 1s for TC2.5 under irradiation shifted positively by 0.2 eV as compared to the

22

values in dark. Accordingly, the binding energies of Cu 2p and In 3d (Figure 6d, e) for TC2.5

showed a negative shift of ca. 0.1 eV under irradiation. Such shifts clearly confirm the

presence of electron transfer from TiO_2 to $CuInS_2$ under light irradiation driven by the direct

Z-scheme heterojunction, agreeing well with the above analyses.

DFT calculations further confirm the generation of the Z-scheme heterostructure

between TiO_2 and $CuInS_2$. Generally, electrons will transfer from the semiconductor with

higher Fermi energy (E_F) level to the other semiconductor with lower E_F level at the interface

of two semiconductors. In our case, the E_F level of $CuInS_2$ is higher than that of TiO_2 (Figure

11). This means the electrons can transfer from $CuInS_2$ to TiO_2 upon contact, creating a

built-in electric field in the TiO_2/$CuInS_2$ interface with the orientation from $CuInS_2$ to TiO_2

upon contact. These analyses agree well with the XPS results as discussed above, that the

electrons transfer from $CuInS_2$ to TiO_2 after hybridization to form a built-in electric field

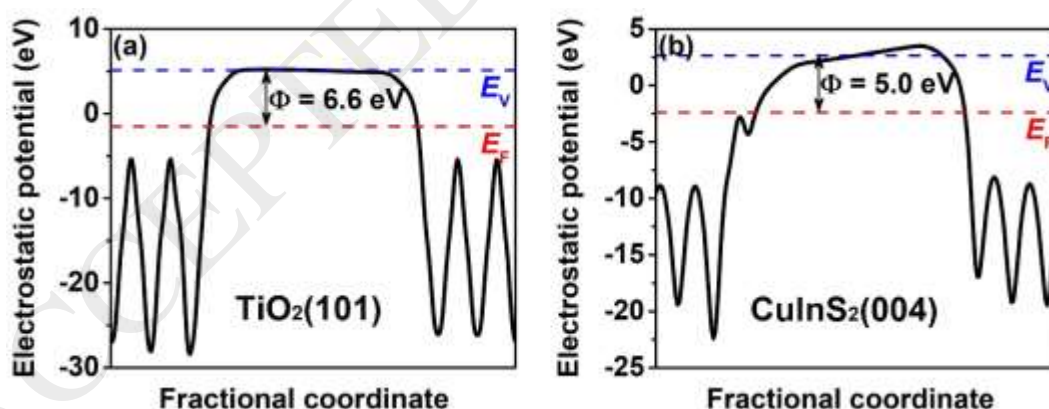resulting from the shift of binding energies of Ti 2p, O 1s, Cu 2p and In 3d.

Figure 11. Calculated electrostatic potentials for (a) TiO_2 (101) face and (b) $CuInS_2$ (004)

face. The red and blue dashed lines denote Fermi level and the vacuum energy level,

respectively.

According to the above results and discussion, we propose a mechanism of the photocatalytic CO_2 reduction upon the hybrid materials. Under light irradiation, the electrons in the valence band (VB) of TiO_2 and $CuInS_2$ were excited to the conduction band (CB). Owing to the presence of the internal electric field pointing from $CuInS_2$ to TiO_2, the electrons in TiO_2 CB would transfer and recombine with the holes in $CuInS_2$ VB, instead of the electrons in $CuInS_2$ CB transfer to TiO_2 CB. This Z-scheme configuration can improve the separation and extraction of the charge carriers (electrons from $CuInS_2$ and holes from TiO_2) [64-66]. Therefore, the photo-induced electrons from $CuInS_2$ CB would react with the adsorbed CO_2 molecules, with the CO_2 reduced to CH_4 and CH_3OH with water as the proton source [67-69]. The photocatalytic mechanism and the charge transfer for the $TiO_2/CuInS_2$ Z-scheme heterostructures are schematically illustrated in Figure 12.
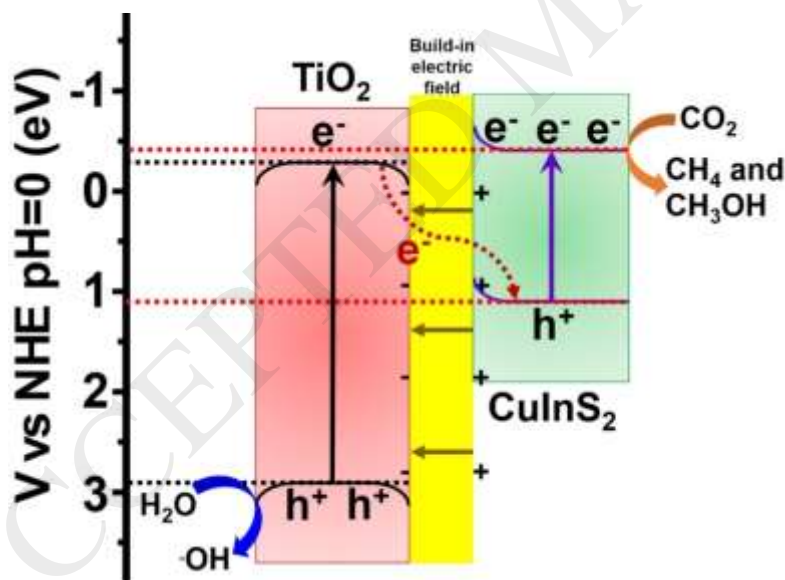

Figure 12. Schematic illustration of the charge transfer and separation in TC2.5 under simulated sunlight light irradiation.

24

4. Conclusions

In summary, novel TiO$_2$/CuInS$_2$ core-shell nanofibers were fabricated through an electrospinning and subsequent hydrothermal methods. The resulting TiO$_2$/CuInS$_2$ hybrid nanofibers exhibit superior photocatalytic activity for CO$_2$ reduction under irradiation, due to the enhanced light absorption, increased surface area and most importantly, the generation of Z-scheme heterojunction between TiO$_2$ and CuInS$_2$. The formation of the Z-scheme heterojunction was verified by XPS measurement, DFT calculation and free radical analysis. The direct Z-scheme heterojunction could significantly promote the charge separation and extraction upon photo-excitation, resulting in improved hydrocarbon production from CO$_2$ reduction. Our work provides a new insight into the design and synthesis of TiO$_2$-based photocatalysts with Z-scheme pathways for high-efficiency solar-fuel conversion.

References

[1] J. Fu, J. Yu, C. Jiang, B. Cheng, g-C$_3$N$_4$-Based Heterostructured Photocatalysts, Adv.

Energy Mater. 8 (2018) 1701503.

[2] W.-H. Wang, Y. Himeda, J.T. Muckerman, G.F. Manbeck, E. Fujita, CO_2 Hydrogenation to Formate and Methanol as an Alternative to Photo- and Electrochemical CO_2 Reduction, Chem. Rev. 115 (2015) 12936-12973.

[3] J. Low, J. Yu, W. Ho, Graphene-Based Photocatalysts for CO_2 Reduction to Solar Fuel, J. Phys. Chem. Lett. 6 (2015) 4244-4251.

[4] W. Tu, Y. Zhou, Z. Zou, Photocatalytic Conversion of CO_2 into Renewable Hydrocarbon Fuels: State-of-the-Art Accomplishment, Challenges, and Prospects, Adv. Mater. 26 (2014) 4607-4626.

[5] J. Jin, T. He, Facile synthesis of Bi_2S_3 nanoribbons for photocatalytic reduction of CO_2 into CH_3OH, Appl. Surf. Sci. 394 (2017) 364-370.

[6] W. Yu, J. Chen, T. Shang, L. Chen, L. Gu, T. Peng, Direct Z-scheme $g-C_3N_4/WO_3$ photocatalyst with atomically defined junction for H_2 production, Appl. Catal. B 219 (2017) 693-704.

[7] T. Di, B. Zhu, B. Cheng, J. Yu, J. Xu, A direct Z-scheme $g-C_3N_4/SnS_2$ photocatalyst with superior visible-light CO_2 reduction performance, J. Catal. 352 (2017) 532-541.

[8] Y. Chen, D. Wang, X. Deng, Z. Li, Metal–organic frameworks (MOFs) for photocatalytic CO_2 reduction, Catal. Sci. Technol. 7 (2017) 4893-4904.

[9] Y. Fu, D. Sun, Y. Chen, R. Huang, Z. Ding, X. Fu, Z. Li, An amine-functionalized titanium metal-organic framework photocatalyst with visible-light-induced activity for CO_2 reduction, Angew. Chem. 51 (2012) 3364-3367.

[10] D. Wang, R. Huang, W. Liu, D. Sun, Z. Li, Fe-Based MOFs for Photocatalytic CO_2

Reduction: Role of Coordination Unsaturated Sites and Dual Excitation Pathways, ACS Catal. 4 (2014) 4254-4260.

[11] F. Xu, W. Xiao, B. Cheng, J. Yu, Direct Z-scheme anatase/rutile bi-phase nanocomposite TiO_2 nanofiber photocatalyst with enhanced photocatalytic H_2-production activity, Int. J. Hydrogen Energ. 39 (2014) 15394-15402.

[12] J. Low, B. Cheng, J. Yu, Surface modification and enhanced photocatalytic CO_2 reduction performance of TiO_2: a review, Appl. Surf. Sci. 392 (2017) 658-686.

[13] A. Nikokavoura, C. Trapalis, Alternative photocatalysts to TiO_2 for the photocatalytic reduction of CO_2, Appl. Surf. Sci. 391 (2017) 149-174.

[14] J. Fu, S. Cao, J. Yu, J. Low, Y. Lei, Enhanced photocatalytic CO_2-reduction activity of electrospun mesoporous TiO_2 nanofibers by solvothermal treatment, Dalton Trans. 43 (2014) 9158-9165.

[15] M. Tahir, B. Tahir, N.A.S. Amin, H. Alias, Selective photocatalytic reduction of CO_2 by H_2O/H_2 to CH_4 and CH_3OH over Cu-promoted In_2O_3/TiO_2 nanocatalyst, Appl. Surf. Sci. 389 (2016) 46-55.

[16] K. Qi, B. Cheng, J. Yu, W. Ho, A review on TiO_2-based Z-scheme photocatalysts, Chin. J. Catal. 38 (2017) 1936-1955.

[17] L.-L. Tan, W.-J. Ong, S.-P. Chai, A.R. Mohamed, Photocatalytic reduction of CO_2 with H_2O over graphene oxide-supported oxygen-rich TiO_2 hybrid photocatalyst under visible light irradiation: Process and kinetic studies, Chem. Eng. J. 308 (2016) 248-255.

[18] Q. Xu, J. Yu, J. Zhang, J. Zhang, G. Liu, Cubic anatase TiO_2 nanocrystals with enhanced photocatalytic CO_2 reduction activity, Chem. Commun. 51 (2015) 7950-7953.

27

[19] J. Yu, J. Low, W. Xiao, P. Zhou, M. Jaroniec, Enhanced Photocatalytic CO_2-Reduction Activity of Anatase TiO_2 by Coexposed {001} and {101} Facets, J. Am. Chem. Soc. 136 (2014) 8839-8842.

[20] P. Kar, S. Farsinezhad, N. Mahdi, Y. Zhang, U. Obuekwe, H. Sharma, J. Shen, N. Semagina, K. Shankar, Enhanced CH_4 yield by photocatalytic CO_2 reduction using TiO_2 nanotube arrays grafted with Au, Ru, and ZnPd nanoparticles, Nano Res. 9 (2016) 3478-3493.

[21] O. Ola, M.M. Maroto-Valer, Synthesis, characterization and visible light photocatalytic activity of metal based TiO_2 monoliths for CO_2 reduction, Chem. Eng. J. 283 (2016) 1244-1253.

[22] M. Tahir, B. Tahir, N.A.S. Amin, Z.Y. Zakaria, Photo-induced reduction of CO_2 to CO with hydrogen over plasmonic Ag-NPs/TiO_2 NWs core/shell hetero-junction under UV and visible light, J. CO_2 Util. 18 (2017) 250-260.

[23] N. Umezawa, H.H. Kristoffersen, L.B. Vilhelmsen, B. Hammer, Reduction of CO_2 with Water on Pt-Loaded Rutile TiO_2(110) Modeled with Density Functional Theory, J. Phys. Chem. C 120 (2016) 9160-9164.

[24] Q. Wang, P. Dong, Z. Huang, X. Zhang, Synthesis of Ag or Pt nanoparticle-deposited TiO_2 nanorods for the highly efficient photoreduction of CO_2 to CH_4, Chem. Phys. Lett. 639 (2015) 11-16.

[25] W. Wang, D. Xu, B. Cheng, J. Yu, C. Jiang, Hybrid carbon@TiO_2 hollow spheres with enhanced photocatalytic CO_2 reduction activity, J. Mater. Chem. A 5 (2017) 5020-5029.

[26] M.S. Akple, J. Low, S. Liu, B. Cheng, J. Yu, W. Ho, Fabrication and enhanced CO_2

28

reduction performance of N-self-doped TiO_2 microsheet photocatalyst by bi-cocatalyst modification, J. CO_2 Util. 16 (2016) 442-449.

[27] V. Trevisan, A. Olivo, F. Pinna, M. Signoretto, F. Vindigni, G. Cerrato, C.L. Bianchi, C-N/TiO_2 photocatalysts: Effect of co-doping on the catalytic performance under visible light, Appl. Catal. B 160 (2014) 152-160.

[28] M.S. Akple, J. Low, Z. Qin, S. Wageh, A.A. Al-Ghamdi, J. Yu, S. Liu, Nitrogen-doped TiO_2 microsheets with enhanced visible light photocatalytic activity for CO_2 reduction, Chin. J. Catal. 36 (2015) 2127-2134.

[29] B. O'Regan, L. Xiaoe, T. Ghaddar, Dye adsorption, desorption, and distribution in mesoporous TiO_2 films, and its effects on recombination losses in dye sensitized solar cells, Energy Environ. Sci. 5 (2012) 7203-7215.

[30] M. Wang, J. Bai, F. Le Formal, S.-J. Moon, L. Cevey-Ha, R. Humphry-Baker, C. Grätzel, S.M. Zakeeruddin, M. Grätzel, Solid-state dye-sensitized solar cells using ordered TiO_2 nanorods on transparent conductive oxide as photoanodes, J. Phys. Chem. C 116 (2012) 3266-3273.

[31] D.O. Adekoya, M. Tahir, N.A.S. Amin, g-C_3N_4/(Cu/TiO_2) nanocomposite for enhanced photoreduction of CO_2 to CH_3OH and HCOOH under UV/visible light, J. CO_2 Util. 18 (2017) 261-274.

[32] J.E. Benedetti, D.R. Bernardo, A. Morais, J. Bettini, A.F. Nogueira, Synthesis and characterization of a quaternary nanocomposite based on TiO_2/CdS/rGO/Pt and its application in the photoreduction of CO_2 to methane under visible light, RSC Adv. 5 (2015) 33914-33922.

[33] Y. Li, W. Zhang, X. Shen, P. Peng, L. Xiong, Y. Yu, Octahedral Cu_2O-modified TiO_2 nanotube arrays for efficient photocatalytic reduction of CO_2, Chin. J. Catal. 36 (2015) 2229-2236.

[34] J. Liu, B. Cheng, J. Yu, A new understanding of the photocatalytic mechanism of the direct Z-scheme g-C_3N_4/TiO_2 heterostructure, Phys. Chem. Chem. Phys. 18 (2016) 31175-31183.

[35] M. Reli, P. Huo, M. Sihor, N. Ambrozova, I. Troppova, L. Matejova, J. Lang, L. Svoboda, P. Kustrowski, M. Ritz, P. Praus, K. Koci, Novel TiO_2/C_3N_4 Photocatalysts for Photocatalytic Reduction of CO_2 and for Photocatalytic Decomposition of N_2O, J. Phys. Chem. A 120 (2016) 8564-8573.

[36] A.Y. Meng, B.C. Zhu, B. Zhong, L.Y. Zhang, B. Cheng, Direct Z-scheme TiO_2/CdS hierarchical photocatalyst for enhanced photocatalytic H_2-production activity, Appl. Surf. Sci. 422 (2017) 518-527.

[37] H. Cao, Y. Zhu, X. Yang, C. Li, Fabrication of $CuInS_2$-TiO_2 composite fibers by using electrospinning coupled with solvothermal method, RSC Adv. 2 (2012) 4055.

[38] S.-Z. Kang, Y.-K. Yang, W. Bu, I. Mu, TiO_2 nanoparticles incorporated with $CuInS_2$ clusters: preparation and photocatalytic activity for degradation of 4-nitrophenol, J. Solid State Chem. 182 (2009) 2972-2976.

[39] J.-H. Yun, Y.H. Ng, S. Huang, G. Conibeer, R. Amal, Wrapping the walls of n-TiO_2 nanotubes with p-$CuInS_2$ nanoparticles using pulsed-electrodeposition for improved heterojunction photoelectrodes, Chem. Commun. 47 (2011) 11288-11290.

[40] T. Li, X. Li, Q. Zhao, Y. Shi, W. Teng, Fabrication of n-type $CuInS_2$ modified TiO_2

nanotube arrays heterostructure photoelectrode with enhanced photoelectrocatalytic

properties, Appl. Catal. B 156 (2014) 362-370.

[41] K. Guo, Z. Liu, J. Han, Z. Liu, Y. Li, B. Wang, T. Cui, C. Zhou, Hierarchical

TiO_2-$CuInS_2$ core-shell nanoarrays for photoelectrochemical water splitting, Phys. Chem.

Chem. Phys. 16 (2014) 16204-16213.

[42] T. Li, X. Li, Q. Zhao, W. Teng, Preparation of $CuInS_2$/TiO_2 nanotube heterojunction

arrays electrode and investigation of its photoelectrochemical properties, Mater. Res. Bull. 59

(2014) 227-233.

[43] M.E. Aguirre, R.X. Zhou, A.J. Eugene, M.I. Guzman, M.A. Grela, Cu_2O/TiO_2

heterostructures for CO_2 reduction through a direct Z-scheme: Protecting Cu_2O from

photocorrosion, Appl. Catal. B 217 (2017) 485-493.

[44] L. Li, T. J. Daou, I. Texier, T. T. Kim Chi, N. Q. Liem, P. Reiss, Highly luminescent

$CuInS_2$/ZnS core/shell nanocrystals: cadmium-free quantum dots for in vivo imaging, Chem.

Mater. 21 (2009) 2422-2429.

[45] I. Tsuji, H. Kato, A. Kudo, Visible-light-induced H_2 evolution from an aqueous solution

containing sulfide and sulfite over a ZnS-$CuInS_2$-$AgInS_2$ solid-solution photocatalyst, Angew.

Chem. 44 (2005) 3565-3568.

[46] Y.J. Yuan, D.Q. Chen, Y.W. Huang, Z.T. Yu, J.S. Zhong, T.T. Chen, W.G. Tu, Z.J. Guan,

D.P. Cao, Z.G. Zou, MoS_2 Nanosheet-Modified $CuInS_2$ Photocatalyst for

Visible-Light-Driven Hydrogen Production from Water, ChemSusChem 9 (2016) 1003-1009.

[47] X. Li, K. Xie, L. Song, M. Zhao, Z. Zhang, Enhanced Photocarrier Separation in

Hierarchical Graphitic-C_3N_4-Supported $CuInS_2$ for Noble-Metal-Free Z-Scheme

Photocatalytic Water Splitting, ACS Appl. Mater. Interfaces 9 (2017) 24577-24583.

[48] S. Luo, J. Ke, M. Yuan, Q. Zhang, P. Xie, L. Deng, S. Wang, $CuInS_2$ quantum dots embedded in Bi_2WO_6 nanoflowers for enhanced visible light photocatalytic removal of contaminants, Appl. Catal. B 221 (2018) 215-222.

[49] M. Baek, E.J. Kim, S.W. Hong, W. Kim, K. Yong, Environmentally benign synthesis of $CuInS_2$/ZnO heteronanorods: visible light activated photocatalysis of organic pollutant/bacteria and study of its mechanism, Photochem. Photobiol. Sci. 16 (2017) 1792-1800.

[50] T. Xu, J. Hu, Y. Yang, W. Que, X. Yin, H. Wu, L. Chen, Ternary system of ZnO nanorods/reduced graphene oxide/$CuInS_2$ quantum dots for enhanced photocatalytic performance, J. Alloys Compd. 734 (2018) 196-203.

[51] J. Yuan, C. Hao, Solar-driven photoelectrochemical reduction of carbon dioxide to methanol at $CuInS_2$ thin film photocathode, Sol. Energy Mater. Sol. Cells 108 (2013) 170-174.

[52] Sing KSW, Everett DH, Haul RAW, Moscou L, Pierotti RA, Rouquerol J, S. T, Reporting physisorption data for gas/solid systems with special reference to the determination of surface area and porosity, Pure Appl. Chem. 57 (1985) 603-619.

[53] G. Yang, D. Chen, H. Ding, J. Feng, J.Z. Zhang, Y. Zhu, S. Hamid, D.W. Bahnemann, Well-designed 3D $ZnIn_2S_4$ nanosheets/TiO_2 nanobelts as direct Z-scheme photocatalysts for CO_2 photoreduction into renewable hydrocarbon fuel with high efficiency, Appl. Catal. B 219 (2017) 611-618.

[54] Y. Wei, J. Jiao, Z. Zhao, W. Zhong, J. Li, J. Liu, G. Jiang, A. Duan, 3D ordered

32

macroporous TiO_2-supported Pt@CdS core–shell nanoparticles: design, synthesis and

efficient photocatalytic conversion of CO_2 with water to methane, J. Mater. Chem. A 3 (2015)

11074-11085.

[55] B. Yu, Y. Zhou, P. Li, W. Tu, P. Li, L. Tang, J. Ye, Z. Zou, Photocatalytic reduction of

CO_2 over Ag/TiO_2 nanocomposites prepared with a simple and rapid silver mirror method,

Nanoscale 8 (2016) 11870-11874.

[56] Z. Xiong, Z. Lei, C.-C. Kuang, X. Chen, B. Gong, Y. Zhao, J. Zhang, C. Zheng, J.C.S.

Wu, Selective photocatalytic reduction of CO_2 into CH_4 over Pt-Cu_2O TiO_2 nanocrystals: The

interaction between Pt and Cu_2O cocatalysts, Appl. Catal. B 202 (2017) 695-703.

[57] A. Razzaq, A. Sinhamahapatra, T.-H. Kang, C.A. Grimes, J.-S. Yu, S.-I. In, Efficient

solar light photoreduction of CO_2 to hydrocarbon fuels via magnesiothermally reduced TiO_2

photocatalyst, Appl. Catal. B 215 (2017) 28-35.

[58] S. Qamar, F. Lei, L. Liang, S. Gao, K. Liu, Y. Sun, W. Ni, Y. Xie, Ultrathin TiO_2 flakes

optimizing solar light driven CO_2 reduction, Nano Energy 26 (2016) 692-698.

[59] M. Yamamoto, T. Yoshida, N. Yamamoto, T. Nomoto, Y. Yamamoto, S. Yagi, H. Yoshida,

Photocatalytic reduction of CO_2 with water promoted by Ag clusters in Ag/Ga_2O_3

photocatalysts, J. Mater. Chem. A 3 (2015) 16810-16816.

[60] J. Szanyi, J.H. Kwak, Photo-catalytic oxidation of acetone on a TiO_2 powder: An in situ

FTIR investigation, J. Mol. Catal. A: Chem. 406 (2015) 213-223.

[61] L. Liu, C. Zhao, J. Xu, Y. Li, Integrated CO_2 capture and photocatalytic conversion by a

hybrid adsorbent/photocatalyst material, Appl. Catal. B 179 (2015) 489-499.

[62] S.N. Habisreutinger, L. Schmidt-Mende, J.K. Stolarczyk, Photocatalytic Reduction of

CO$_2$ on TiO$_2$ and Other Semiconductors, Angew. Chem., Int. Ed., 52 (2013) 7372-7408.

[63] L. Liu, Y. Li, Understanding the Reaction Mechanism of Photocatalytic Reduction of CO$_2$ with H$_2$O on TiO$_2$-Based Photocatalysts: A Review, Aerosol Air Qual. Res. 14 (2014) 453-469.

[64] Y. Fu, Z. Li, Q. Liu, X. Yang, H. Tang, Construction of carbon nitride and MoS$_2$ quantum dot 2D/0D hybrid photocatalyst: Direct Z-scheme mechanism for improved photocatalytic activity, Chin. J. Catal. 38 (2017) 2160-2170.

[65] S. Song, A. Meng, S. Jiang, B. Cheng, C. Jiang, Construction of Z-scheme Ag$_2$CO$_3$ /N-doped graphene photocatalysts with enhanced visible-light photocatalytic activity by tuning the nitrogen species, Appl. Surf. Sci. 396 (2017) 1368-1374.

[66] Z. Wang, T. Hu, K. Dai, J. Zhang, C. Liang, Construction of Z-scheme Ag$_3$PO$_4$ /Bi$_2$WO$_6$ composite with excellent visible-light photodegradation activity for removal of organic contaminants, Chin. J. Catal. 38 (2017) 2021-2029.

[67] J. Low, J. Yu, M. Jaroniec, S. Wageh, A. Al-Ghamdi, Heterojunction Photocatalysts, Adv. Mater. 29 (2017) 1601694..

[68] P. Zhou, J. Yu, M. Jaroniec, All-Solid-State Z-Scheme Photocatalytic Systems, Adv. Mater. 26 (2014) 4920-4935.

[69] J. Low, C. Jiang, B. Cheng, S. Wageh, A.A. Al-Ghamdi, J. Yu, A Review of Direct Z-Scheme Photocatalysts, Small Methods 1 (2017) 1700080.

Table 1. Physical properties of the samples

Samples	CuInS$_2$ (mol%)	S_{BET} (m^2/g)	PV (m^3/g)	APS (nm)
T	-	43	0.14	10
TC1	1.4	68	0.18	10.4
TC2.5	3.1	102	0.45	17.6
TC5	5.2	83	0.45	21.5
TC10	9.4	51	0.25	20.1

PV: pore volume, APS: average pore size